Insights into the Self-Assembly and Interaction of SARS-CoV-2 Fusion Peptides with Biomimetic Plasma Membrane Models

Nisha Pawar[1,2], Andreas Santamaria[3], Krishna C. Batchu[3], Eduardo Guzman[4,5], Nathan. R. Zaccai,[6] Alberto Alvarez-Fernandez,[1,*] Armando Maestro.[1,7,*]

[1] *Centro de Física de Materiales (CFM) (CSIC–UPV/EHU) – Materials Physics Center (MPC), Paseo Manuel de Lardizabal 5, San Sebastián, 20018 Spain*

[2] *Institute for Bioengineering of Catalonia, The Barcelona Institute of Science and Technology, Barcelona 08028, Spain*

[3] *Institut Laue-Langevin, 71 Avenue des Martyrs, 38042 Grenoble, Cedex 9, France.*

[4] *Departamento de Química Física, Facultad de Ciencias Químicas, Universidad Complutense de Madrid, Ciudad Universitaria s/n, 28040, Madrid, Spain*

[5] *Instituto Pluridisciplinar, Universidad Complutense de Madrid, Paseo Juan XXIII 1, 28040, Madrid, Spain*

[6] *Cambridge Institute for Medical Research, University of Cambridge, Cambridge CB2 0XY, United Kingdom.*

[7] *IKERBASQUE-Basque Foundation for Science, Plaza Euskadi 5, Bilbao, 48009, Spain*

*E-mail address: alberto.alvarez@ehu.eus; armando.maestro@ehu.eus

Abstract

The COVID-19 pandemic, which was caused by SARS-CoV-2, initiated a global health crisis in 2019. SARS-CoV-2 is a single-stranded RNA virus encased in a lipid envelope that houses key structural proteins, including the Spike glycoprotein, which mediates viral entry into host cells. Within the Spike protein, the S2 subunit, and particularly its fusion domain, plays a critical role in merging viral and host membranes. Understanding the fusion domain interactions at the molecular level is important for advancing applications such as the development of novel antiviral therapies. This study investigates the self-assembly of SARS-CoV-2 S2 subunit fusion peptides (FPs) and their interaction with biomimetic plasma membrane (PM) models composed of physiological mixes of phospholipids, sphingomyelin, and cholesterol. Complementary techniques, including atomic force microscopy, neutron reflectometry and grazing incidence X-ray diffraction, provided detailed insights into lipid nano-mechanics and in-plane molecular structure. Our findings reveal several types of FP assemblies at the PM interface, including the formation of rigid fibres, spiral structures, and segregated domains. These behaviours are influenced by FP intrinsic features such as hydrophobicity and molecular structure, and the resultant interactions with lipid headgroups and tail regions. This work enhances our molecular-level understanding of FP-lipid interactions, shedding light on viral entry mechanisms. Furthermore, the ability of these peptides to self-assemble, modulated by the surrounding lipid environment, positions them as promising building blocks for innovative functional biomaterials.

1. Introduction:

Fusion peptides (FPs) from the SARS-CoV-2 Spike (S) protein are critical for the virus's entry into host cells.[1,2] These short peptide sequences, located within the spike protein´s fusion domain, exhibit unique properties that facilitate their insertion into and interaction with lipid bilayers, enabling the merging of viral and host cell membranes,[3–5] and ultimately viral infection. Beyond their biological relevance in viral entry, SARS-CoV-2 FPs have also shown promise as building blocks for the fabrication of novel functional nanomaterial.[6] Their probed ability to self-assemble into well-defined nanostructures at fluid interfaces offers opportunities

for designing novel chiral nanomaterials with expected applications in biomedicine and nanotechnology.

Structurally, the Spike protein consists of two subunits, S1 and S2, each with distinct roles in viral infection.[7] The S1 subunit primarily facilitates the virus´s initial attachment to the host cell by binding to its receptors. In contrast, the S2 subunit drives the subsequent membrane fusion process, allowing the viral genome to enter the host cell.[8] Concretely, within the S2 subunit, a critical region known as the fusion domain interacts directly with the host cell´s lipid bilayer,[9] disrupting and connecting opposing membranes to merge the viral and host membranes.[10] Intermolecular interactions between specific sections of the fusion domain, claaed "fusion peptides" (FP), and the lipid bilayer are fundamental in regulating this process.[11] By embedding into the lipid bilayer, FP induce membrane destabilization, creating an initial point of contact that promotes the merging of the viral and host cell membranes. The expected characteristics of FP—short, hydrophobic, and potentially containing canonical fusion tripeptides (such as YFG or FXG)—along with a central proline residue, have led to the identification of several putative SARS-CoV-2 fusion peptides. Specifically, these sequences include FP1 (residues 816–837), FP2 (835–856), and FP4 (885–909), the latter is also commonly referred as the internal fusion peptide. Moreover, these peptides are not only integral to the fusion process but have also been identified as targets for broadly neutralizing antibodies against all known human-infecting coronaviruses. These molecules are therefore promising targets for the development of universal coronavirus vaccines,[12,13].

Given this intrinsic ability to interact with and perturb lipid membranes, FPs serve as ideal candidates for studying self-assembly and peptide-lipid interactions. Exploring their behaviour at membrane interfaces can enhance our understanding of viral entry mechanisms while inspiring the development of biomimetic nanomaterials for applications such as drug delivery and biosensing.

Lipid Langmuir-Blodgett (LB) monolayers provide a controlled platform to study peptide – membrane interactions at the molecular level, through precise control over structural lipid order and phase regimes through monolayer compression.[14,15] The monolayers are simplified representations of biological membranes. In earlier work, we revealed that different SARS-CoV-2 fusion peptides perform distinct functions on interaction with monolayer models of the plasma membrane (PM).[11] However, further in-depth investigations are required to fully

elucidate the self-assembly of FPs and their pivotal role in orchestrating the viral fusion mechanism, which remains elusive.

Here, we investigate the self-assembly of SARS-CoV-2 FPs incubated with lipid mixtures mimicking the outer leaflet of the eukaryotic plasma membrane (PM), creating hybrid peptide-lipid Langmuir monolayers. These PM models are characterized by a high cholesterol content (50 mol %), and include sphingomyelin, the zwitterionic phospholidpids, phosphatidylcholines (PC) and phosphatidylethanolamines (PE), as well as lower proportions of anionic lipids phosphatidylserines (PS) and phosphatidylinositols (PI).[16] By compressing the PM monolayer in a Langmuir-Blodgett (LB) trough, the packing density of the lipids can be controlled, simulating the restricted packing that occurs in a membrane leaflet under biologically relevant conditions. Grazing incidence X-ray diffraction (GIXD) and atomic force microscopy (AFM) were employed to elucidate the in-plane molecular organization and lipid packing within the PM monolayer, as well as the surface morphology following FP association. These techniques revealed different FP assemblies at the PM interface, including the formation of rigid fibres, spiral structures, and segregated domains.

This study also highlights the potential of hybrid peptide-lipid monolayers as versatile platforms for exploring and fine-tuning peptide-driven assembly. These systems offer a foundation for designing advanced biomimetic materials with applications in drug delivery, biosensing, and membrane engineering.

2. Materials and Methods:

***Fusion Peptides*:** The fusion peptides were synthesized and purified by GenScript (Amsterdam, The Netherlands). Stock solutions of each peptide in DMSO (dimethyl sulfoxide) were used for all the experiments reported here. The following peptides were investigated: FP1 (SARS-CoV-2 816-SFIEDLLFNKVTLADAGFIKQY- 837); FP2 (SARS-CoV-2 835-KQYGDCLGDIAARDLICAQKFN- 856); and FP4 (SARS-CoV-2 885-GWTFGAGAALQIPFAMQMAYRFNGI- 909). See **Table S1** for further details of the peptides.

Hybrid FPs – lipid mixture solutions preparation and Biomimetic PM Formulation: Outer leaflet of eukaryotic plasma membranes was prepared in the form of Langmuir monolayers as detailed elsewhere.[17,18] Briefly, phosphatidylcholine (PC), phosphatidylethanolamine (PE) and

phosphatidylserine (PS) extracted and purified from perdeuterated and hydrogenous *Pichia pastoris* cell cultures were mixed by cholesterol and egg yolk sphingomyelin purchased in powder form from Sigma-Aldrich. The composition in molar ratio was PC 0.2, PE 0.11, PS 0.06, cholesterol 0.5, sphingomyelin 0.13 (**Table S2**). Lipid stock solutions were prepared in chloroform stabilized with ethanol (purity 99.8%; Sigma Aldrich, St. Louis, MO, USA), and stored at -20°C. Mixed solutions of lipids and peptides (PM-FP) were prepared by adding 5% moles (*i.e.*, 1:20 FP:lipid) of FP to the PM solutions. The final lipid concentration used in all solutions was maintained at 0.2 mg/mL.

***Langmuir trough experiments*:** Surface pressure (Π) − area (A) isotherms of hybrid PM-FPs monolayers were acquired using a LB trough (model G2, KIBRON, Helsinki, Finland). Surface pressure variation was recorded using a Wilhelmy plate made of filter paper. The temperature was maintained at 21.5 ± 0.5 °C. The trough was filled with de-ionized water (Milli-Q, Millipore; resistivity higher than 18 MΩ·cm), and freshly cleaved mica substrates were vertically immersed using a dipper. A 0.2 mg/mL lipid mixture (PM), in chloroform was spread over the subphase using a Hamilton micro-syringe, achieving an initial surface pressure of 2 mN/m. After chloroform evaporation (20 min) surface pressure variations during compression were recorded using the Wilhelmy plate. Once the target surface pressure (20 and 35 mN/m) was reached, the interfacial assemblies were transferred onto mica substrate (discs with 12 mm of diameter). Similar protocol was followed for 0.2 mg/ml Lipid mixture+ 5% FP1, 0.2 mg/ml Lipid mixture+ 5% FP2, 0.2 mg/ml Lipid mixture+ 5% FP2 monolayers.

***Area per molecule calculation by Neutron reflectometry*:** Quantification of the membrane composition was done by neutron reflectometry (NR) exploiting the low-q_z-range approach, *i.e.*, by collecting data at a limited q_z-range, 0.01 $Å^{-1} < q_z < 0.03$ $Å^{-1}$ (λ from 4.5 to 13 Å), which allows a relatively fast acquisition time. NR experiments were performed on the time-of-flight reflectometer FIGARO at the Institut Laue-Langevin, Grenoble (France).[19] Only the lowest angle of incidence (θ = 0.6°) was used for the experiments, and a wavelength resolution of 7% dλ/λ. The raw time-of-flight experimental data were normalized with respect to the incident wavelength distribution and the efficiency of the detector yielding the resulting R(Q_z) profile using COSMOS.[20] A one-layer model of the PM and PM-FP monolayers, respectively (**Table S3**) was used to determine the area per molecule (A) of phospholipids and fusion peptides at different values of Π following previous studies (**Figure S1**).[21] The are per molecule is given by $A = {\sum b_i}/{\rho_i \cdot t}$, where $\sum b_i$ and ρ_i are the scattering length and the scattering length density

of each component, respectively, and t is the film thickness (**Table S4**). The data analysis was performed by fitting the product of $\sum \rho_i$ and t. This was done for deuterated PM monolayers in presence/absence of FPs in D_2O:H_2O mixture (8:92% v/v) subphase. In the fitting process performed using REFNX,[22] the interfacial roughness was fixed to 3 Å, which is consistent with the capillary waves of the subphase.[23,24]

Atomic Force Microscopy: The monolayer formed by PM in the absence and presence of FP were imaged at the air-solid interface by AFM. All images were obtained with a multimode AFM and a Nanoscope V controller (Bruker). The AFM was operated in Peak Force mode, at room temperature.[25] Silicon nitride cantilevers (model: PNP/DP) with force constant 0.48 N/m, length 100 μm and a resonant frequency of 67kHz, were used for scanning. The images were taken at a scan rate of 1 Hz and 512 × 512 pixels. The images were acquired with the Nanoscope Software. They were topologically flattened and analysed by using WSxM software.[26] Nanomechanical properties were determined in the peak force QNM mode of AFM. The advantage of using peak force QNM is that the adhesive force between the sample and tip and the magnitude of sample deformation caused by the tip are both directly measured in real-time. The cantilever was calibrated well using the standard hard surface (sapphire) and images were analysed using NanoScope Analysis software (V1.9, Bruker).

Grazing Incidence X-ray Diffraction (GIXD) experiments were performed at ID 10 beamline at the European Synchrotron Radiation Facility (ESRF), Grenoble, France, with X-ray energy 22keV and a beam size of 25 x 13 μm^2. This technique has been extensively described elsewhere.[27,28] Here, an in-house, setup consisting of a PTFE Langmuir trough equipped with a single moveable barrier, was used for GIXD experiments. The experiment was performed at two selected pressures (20 and 35 mN/m) and at a constant subphase temperature of 21± 0.5 ^{0}C. To minimize the background scattering, the trough was isolated in a Kapton box, and the inside atmosphere was saturated in He (oxygen level < 0.2%). Different areas of the trough were exposed to the X-ray beam in each particular experiment to avoid damage to the sample.[27]

For GIXD experiments, Langmuir monolayers were irradiated with an 8keV X-ray beam at an incidence angle of $\theta = 0.1233°$, 80% below the critical angle of pure water. GIXD 2D contour profiles of the scattered intensity were acquired using a double linear detector (Mythene 2K) mounted behind a vertically oriented Sollers collimator with an in-plane angular resolution of 1.4 mrad. Diffracted intensities were detected as a function of the X-ray momentum transfer component perpendicular, q_z, and parallel to the air/water interface, $q_{xy}=(4\pi/\lambda)\sin 2\theta_{xy}/2$. GIXD peaks were obtained by the integration of the 2D profiles along q_z to obtain the Bragg

peaks using in-house scripts developed at ESRF ID10. These data were fitted using the Lorentzian function in order to obtain the peak position and its full-width half maxima (FWHM). In-plane coherence length (L_{xy}) along the crystallographic direction was determined using the Scherrer formula: $L_{xy} = (0.9 \times 2\pi)/FWHM$.

3. Results and Discussion.

The direct self-assembly of three different peptides derived from the SARS-CoV-2 Spike fusion domain—FP1, FP2, and FP4 (**Figure 1A**)—was investigated in the presence of lipid Langmuir monolayers mimicking the outer leaflet of the eukaryotic PM (**Figure 1B**). The general methodology used in this study is outlined in **Figure 1C**. Lipid monolayers, prepared with and without the incorporation of FPs, were formed using the LB trough at the air/water interface. Uniaxial compression within the LB trough affected peptide-lipid interactions, enabling precise tuning of lipid packing density and facilitating the control of peptide self-organization at the interface. These monolayers were concurrently characterized *in situ* with neutron reflectometry (NR) and GIXD to assess their structural organization. The monolayers were then transferred onto freshly cleaved mica surfaces for AFM analysis in order to evaluate topographical and physico-chemical properties.

3.1. Impact of Fusion Peptides on Lipid Packing in the Outer Leaflet of the Plasma Membrane

The phase behavior of PM and hybrid PM-FPs monolayers at the air-water interface was studied by the surface pressure (Π) - area per molecule (A) isotherms, as shown in **Figure 1D**, by combining a LB trough with low Q_z NR measurements (**Figure S1**). The lateral compressibility of the monolayer was determined from the slope of the Π-A isotherm. This monolayer intrinsic property, commonly expressed in terms of the compressional elastic modulus[29] defined as $C_s^{-1} = -A(\partial\Pi/\partial A)$, is shown in **Figure 1E**.

At low surface pressures, the PM monolayer exhibits an intrinsically disordered, fluid phase commonly referred to as the liquid-expanded (LE) phase. In this phase, the compressional elastic modulus remains relatively constant, with $C_s^{-1} \approx 74 \pm 3$ mN/m regardless of surface pressure. A discontinuity in the compression isotherm observed at $\Pi \approx 20$ mN/m suggests a transition to a condensed (C) phase, likely driven by tighter lipid packing and enhanced lateral interactions as the available molecular area decreases. In the C phase, the elastic modulus significantly increases with surface pressure, following a trend of $C_s^{-1} \approx 6\Pi$, reflecting stronger

lipid-lipid interactions and reduced molecular mobility as the monolayer becomes more ordered.

The incorporation of FPs significantly alters the Π-A isotherm of the PM monolayer (**Figure 1D**). For all three FPs studied (FP1, FP2, and FP4), the isotherm shifts to higher values of the area per molecule, indicating their interaction with the PM. This expansion suggests that the FPs intercalate into the monolayer, disrupting lipid packing and increasing the molecular area. This behaviour can be attributed to a combination of factors, including the insertion of hydrophobic peptide regions into the lipid acyl tails, interactions between charged peptide residues and lipid headgroups, and the potential peptide aggregation or supramolecular assembly within the monolayer.

In comparison to FP2, FP1 and FP4 exhibit stronger interactions with the PM, as evidenced by greater isotherm expansion as well as with previously published binding affinities of these FPs with PM model membranes.[11] FP1 would interact favourably with both lipid headgroups and acyl chains due its overall negative charge at physiological pH, as well as its hydrophobic residues (e.g., phenylalanine, leucine). The positively charged FP4, due to the presence of lysine and arginine residues, would interact strongly with the anionic PS and PI lipid headgroups**.** In contrast, FP2's neutral net charge limits its electrostatic interactions with charged lipid headgroups. Additionally, its cysteine residues may form inter-peptide disulphide bonds **,** introducing conformational constraints that reduce its adaptability to the lipid environment. These factors reduce FP2's capacity to integrate into and perturb the PM monolayer, leading to a less pronounced isotherm expansion.

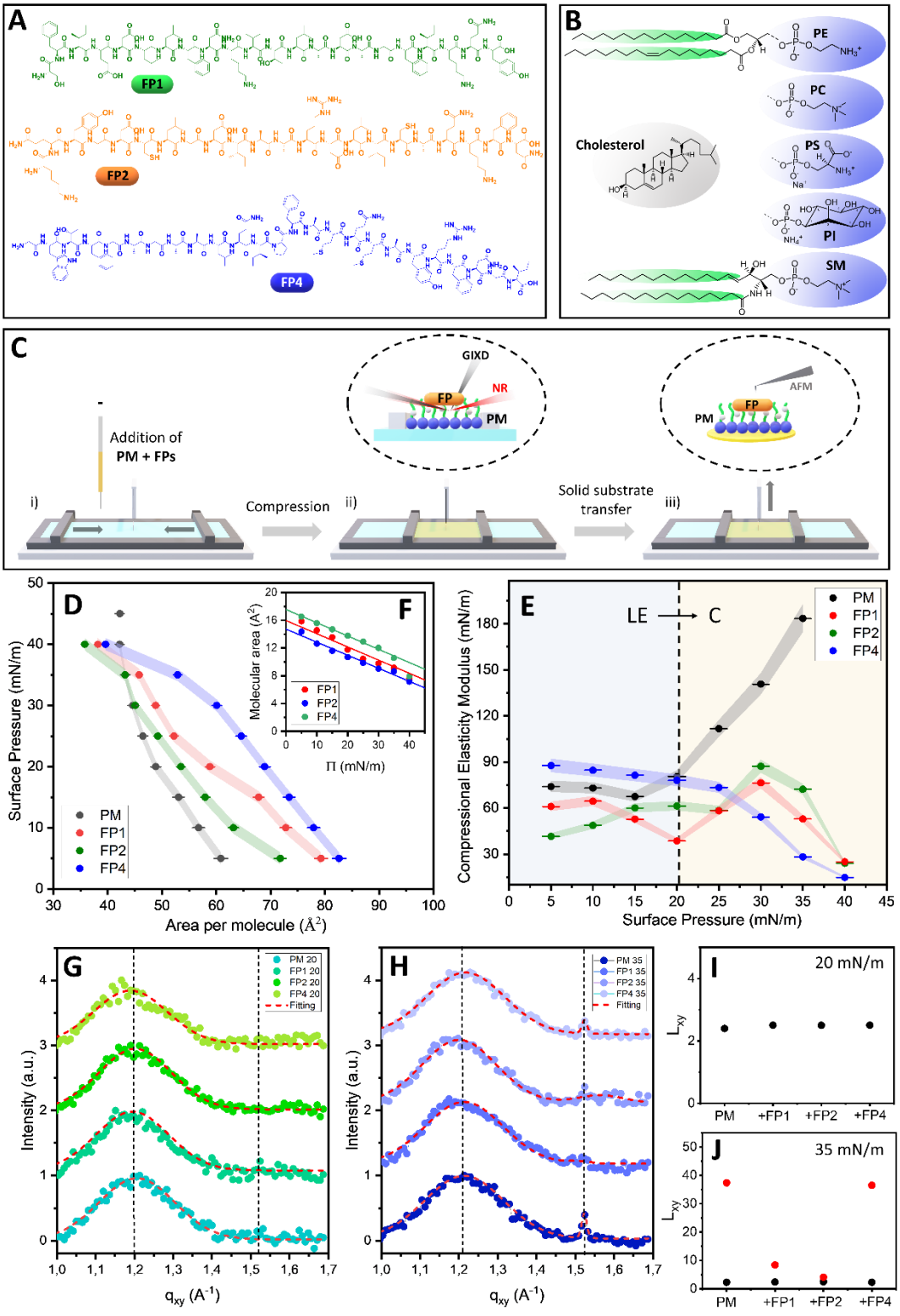

Figure 1. Chemical structure of the peptides (A) and lipids (B) used during this work. Schematic representation of the PM monolayer fabrication and the characterization techniques used during this study (C). Π-A compression isotherm (D) and compression modulus (E) for the PM in the absence and presence of FP1, FP2 and FP4 spread at the air/water interface. FPs

molecular area calculations (F). Variation of diffracted intensity as a function of in-plane scattering vector component (q_{xy}) of PM, PM-FP1, PM-FP2 and PM-FP4 at a surface pressure of 20 mN/m (G) and 35 mN/m (H) and corresponding calculated Lxy (I, J).

The compressional elasticity data (**Figure 1E)** further show the peptides' disruptive effect. In the presence of FPs, the PM monolayers remain in the LE phase across the entire surface pressure range. This persistent fluidity arises from the peptides´ interference with lipid packing, introducing steric hindrance and preventing tight packing. Additionally, the amphipathic nature of the FPs would allow for partial peptide insertion into the monolayer, as observed previously by NR,[11] and leading to increased membrane disorder and fluidity. The interplay between hydrophobic residues inserting into the lipid tails and hydrophilic residues interacting with the aqueous subphase creates a dynamic environment that inhibits the transition to a C phase**.** Despite their differences in charge and sequence, all three FPs consistently modulate the properties of the PM monolayer, underscoring their universal ability to disrupt lipid organization and maintain monolayer fluidity.

To gain deeper insights into the in-plane organization of the PM monolayer in the presence of FPs, GIXD measurements were conducted using synchrotron radiation. Data were collected for PM monolayers with and without FPs at two different surface pressures of Π = 20 mN/m and Π = 35 mN/m, corresponding to the LE and C phases, respectively. These phases are respectively characterized by relatively low and by high compressibility moduli of the PM monolayer. The GIXD intensity contour maps as functions of q_{xy} and q_z for the studied monolayers are presented in **Figure S2** and **S3**, with the corresponding Bragg peaks along q_{xy} shown in **Figures 1G** and **1H** for surface pressures of 20 mN/m and 35 mN/m, respectively.

A diffuse, broad Bragg peak centered at q_{xy} = 1.20 ±0.02 $Å^{-1}$ is observed at both surface pressures (**Figures 1G** and **1H)** indicating limited short-range crystallinity within the monolayer. The calculated in-plane correlation length (L_{xy}) is 24.5 ± 0.5 Å at 20 mN/m and decreases slightly to 23.0 ± 0.5 Å at 35 mN/m (**Figure 1G**, **Table 1**). This diffraction peak is characteristic of cholesterol monolayers, which dominates the PM lipid mixture´s (≈ 50 % mol).[30] The existence of this Bragg peak suggests that cholesterol molecules organize perpendicular to the interface in a hexagonal 2D lattice, consistent with prior GIXD studies**.**[31,32] Further support for this interpretation comes from the Bragg rod, which a maximum near the horizon ($q_z \approx 0.05$ $Å^{-1}$, See **Figure S4**), confirming the perpendicular orientation of cholesterol

molecules relative to the air/water interface. The slight reduction in L_{xy} with increasing Π is attributed to compression-induced rearrangements of cholesterol molecules, reflecting their dominance in the lipid composition of the PM monolayer.

At the higher surface pressure of Π = 35 mN/m (corresponding to the membrane in a C phase), two distinct diffraction peaks are observed (**Figure 1H**). The first peak, centered at $q_{xy} \approx 1.20$ $Å^{-1}$ corresponds to the cholesterol-rich domains and remains consistent with observations at lower surface pressures. A second, weaker diffraction peak emerges at $q_{xy} = 1.52 \pm 0.02$ $Å^{-1}$, which likely corresponds to a hexagonal arrangement of lipid chains from the other lipids (PC, PE, PS and possibly SM), indicating enhanced packing at higher pressures.[33,34] Parameters of the crystal lattices are reported in **Table 1** and **Figure 1I** and **1H**. The L_{xy} for this lipid arrangement is 374 ± 1 Å, significantly larger than the L_{xy} calculated for the cholesterol domains. This suggests that while cholesterol's rigid, bulky structure inherently limits long-range order, the more flexible acyl chains of phospholipids enable tighter packing and higher in-plane coherence. The coexistence of these two Bragg peaks reflects phase separation within the monolayer: cholesterol-rich regions coexisting with more ordered domains of the other lipids. This separation is reinforced by compression, which promotes the organization of the phospholipid components while maintaining the short-range order typical of cholesterol. Such observations are consistent with prior reports on Langmuir monolayers of PE and cholesterol mixtures, where distinct crystalline domains were similarly detected.[35]

Interestingly, at both Π of 20 mN/m and 35 mN/m, the Bragg peak at $q_{xy} \approx 1.20$ $Å^{-1}$, associated with the cholesterol-rich domains, remains unchanged in the presence of FP1, FP2 and FP4 (**Figure 2C, D**). This invariance suggests that these FPs do not directly interact with the ordered cholesterol domains. However, at Π = 20 mN/m, all FPs induce an increase in the L_{xy} of the cholesterol lattice, suggesting the FPs have a subtle influence on lipid short-range order. At Π= 35 mN/m, this effect is less pronounced, with FP4 showing no measurable impact in L_{xy} (see **Table 1**). These results suggest that, while FPs do not disrupt cholesterol packing, their presence at lower surface pressures may stabilize the cholesterol lattice by influencing the surrounding lipid environment. Conversely, at higher Π, the denser packing of lipids likely limits such interactions, particularly for FP4, which appears to integrate into the monolayer without altering cholesterol order. These observations align with theoretical studies indicating that the SARS-CoV-2 FPs have minimal interaction with cholesterol, instead exhibiting a stronger affinity for the other phospholipids present in the membrane.[36]

The position of this second diffraction peak (q_{xy} = 1.52 Å^{-1}) corresponds to the arrangement of the acyl chains of non-cholesterol lipids. At Π = 35 mN/m, it remains unchanged in the presence of FPs. However, significant differences are observed in the peak's intensity and corresponding L_{xy}. Specifically, while the peak is detectable in all cases, its intensity is markedly reduced in the presence of FP1 and FP2, compared to both apo and FP4 associated PM (**Figure 2B**). These results suggest that FP1 and FP2 disrupt the in-plane organization of the PM, by interacting strongly with the lipid acyl chains. This disruption hinders the ability of the lipids to organize into ordered structures. In contrast, FP4 causes less disturbance to the lipid organization as it primarily interacts with lipid head groups and not with their acyl chains. FP4 is therefore associated with formation of more ordered lipid domains, allowing for the preservation of lipid domain structure.

Table 1. Structural parameters obtained from the GIXD analysis for the samples studied during this work.

Π =20mN/m					
	qxy ±0.02 **(Å^{-1})**	**qz** ±0.02 **(Å^{-1})**	**a,b** ± 0.05 **(a=b)(Å)**	**Area (Å^2)**	**Lxy** ± 0.1 **(nm)**
PM	1.21	0.05	6.01	31.3	2.4
PM-FP1	1.20	0.05	6.07	31.9	2.5
PM-FP2	1.20	0.05	6.03	31.5	2.5
PM-FP4	1.19	0.06	6.09	32.2	2.5
Π = 35mN/m					
PM	1.21 1.52	0.050	5.29	27.4	2.3 37.4
PM-FP1	1.21 1.52	0.051	5.31	27.5	2.4 8.4
PM-FP2	1.20 1.52	0.052	5.29	27.7	2.5 4.1
PM-FP4	1.22 1.52	0.051	5.28	27.3	2.3 36.5

3.2. Atomic Force Microscopy analysis of the phase behaviour and lipid organization in PM Monolayers under compression y

To investigate the in-plane lipid organization of PM monolayers in the absence of FPs, AFM was conducted using Langmuir-Blodgett (LB) films as PM models. These monolayers were prepared at selected Π of 20 mN/m and 35 mN/m, which corresponds to the LE and C phases of the outer leaflet of the PM membrane, respectively. AFM micrographs of the pristine PM LB monolayer transferred onto freshly cleaved mica substrates at these surface pressures are presented in **Figures 2A** and **2C**.

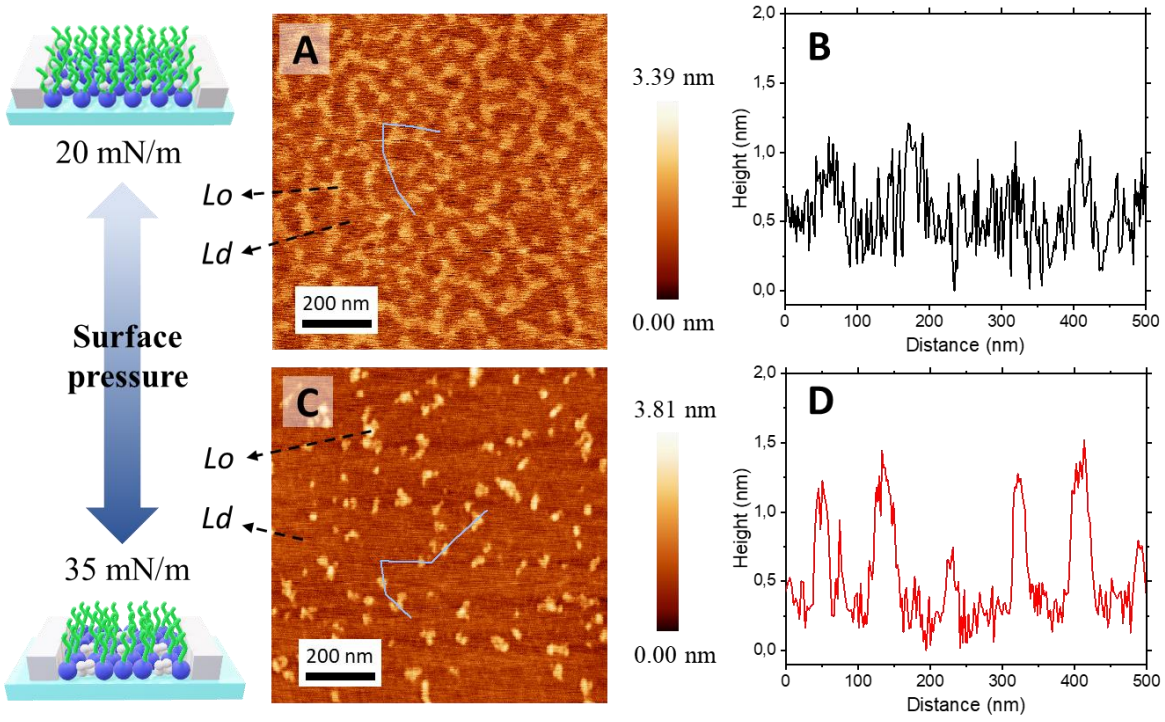

Figure 2. Visualization of Lipid Organization Under Compression: AFM topographical micrographs and corresponding topographical profiles of the pristine PM monolayer at Π of 20 mN/m (A, B) and 35 mN/m (C, D). Schematic representations of the corresponding AFM images are also presented for clarity.

The AFM topographical micrograph of the pristine PM monolayer at Π = 20 mN/m (**Figure 2A**) confirms its structural integrity and reveals a surface roughness of approximately 1 nm (**Figure 2B**). This roughness indicates the presence of two different regions within the monolayer, suggesting lateral phase separation. These regions correspond to the coexistence of two liquid phases: the liquid-ordered (*Lo*) phase and the liquid-disordered (*Ld*) phase.[37] The *Lo* phase is characterized by high lipid packing, primarily driven by strong cohesive van der Waals interactions between the hydrophobic regions of cholesterol and SM. These interactions create tightly packed, less fluid domains enriched in cholesterol and SM, which appear as brighter areas in the AFM micrograph. In contrast, the *Ld* phase, represented by darker regions, is more disordered and fluid, with a composition predominantly consisting of PE, PC and PS, resulting in a lower cholesterol content. The differences in lipid composition and molecular interactions contribute to the lateral heterogeneity observed in the monolayer.[11,35,38]

At Π = 35 mN/m, compression of the PM monolayer reduces the available molecular area, intensifying steric and van der Waals interactions among lipid molecules and bringing them into closer proximity, thereby limiting their lateral mobility. This compression triggers

structural rearrangements, transitioning the PM into a more condensed phase.[11] AFM at this lateral pressure (**Figure 2C**) and corresponding topographical profile (**Figure 2D**) reveal that the bright, *Lo* nanodomains become smaller, more densely packed, and distributed more randomly across the monolayer. The increased concentration and irregular spatial arrangement of *Lo* domains likely result from a balance between domain coalescence, which is energetically favorable, and the spatial constraints imposed by compression. These constraints inhibit domain growth, leading to a fragmented organization.

This phase behavior can be explained by the thermodynamics of lipid packing under compression. At higher Π, the system reduced its free energy by increasing molecular packing density, stabilizing the *Lo* domains. However, the spatial constraints imposed by compression limit the available area for lipid molecules, favoring the formation of smaller, densely packed *Lo* domains rather than large-scale contiguous ones. The randomization of *Lo* domains distribution under compression indicates a disruption of the pre-existing spatial organization. This suggests that smaller, fragmented domains are energetically more favorable in this regime. The interplay between reducing free energy through tighter molecular packing and minimizing line tension —associated with the boundaries between the *Lo* and *Ld* phases—drives this organization. Smaller, randomly distributed *Lo* domains reduce the cumulative line tension while maintaining the phase separation characteristic of the PM monolayer, achieving an optimal balance at higher surface pressures.

3.3 Self-assembly of Fusion Peptides on PM Monolayers revealed by Atomic Force Microscopy

To investigate the in-plane self-assembly of FPs and their impact on lipid organization, AFM was employed to study LB monolayers with a PM composition incorporating FPs. These FPs-PM monolayers, spread at the air/water interface, were transferred onto freshly cleaved mica surfaces at selected surface pressures (Π = 20 and 35 mN/m). Topographical AFM micrographs illustrating the different self-assembled structures of FPs at the PM LB interface are shown in **Figures 3 - 4**.

3.3.1.- Straight and Stiff: Formation of Linear Peptide Fibers by FP1 on PM Monolayers

At Π = 20 mN/m, FP1 self-assembles on the PM monolayer to form long nanofibres, ranging in length from 100 nm to 700 nm, and distributed across the monolayer (**Figure 3A, Figure S5A**). The distribution of fibril heights, with an average value of H = 1.0 ± 0.2 nm, is consistent with a peptide fibrillar structure, where the backbones are aligned parallel to the surface plane and are in contact with the lipid acyl chain region of the PM monolayer. This conformation is

further supported by molecular size calculations for FP1, assuming a β-strand structure, which predict dimensions of approximately 7.4 nm in length and 1.3 nm in height. Previous studies .0have shown that the high β-sheet content of these short peptides at the bare air-water interface promotes the formation of long and uniform fibers under uniaxial compression forces.[6] Similar systems, such as HIV-1 FPs, are also known to form long fibers at the air-water interface.[39]

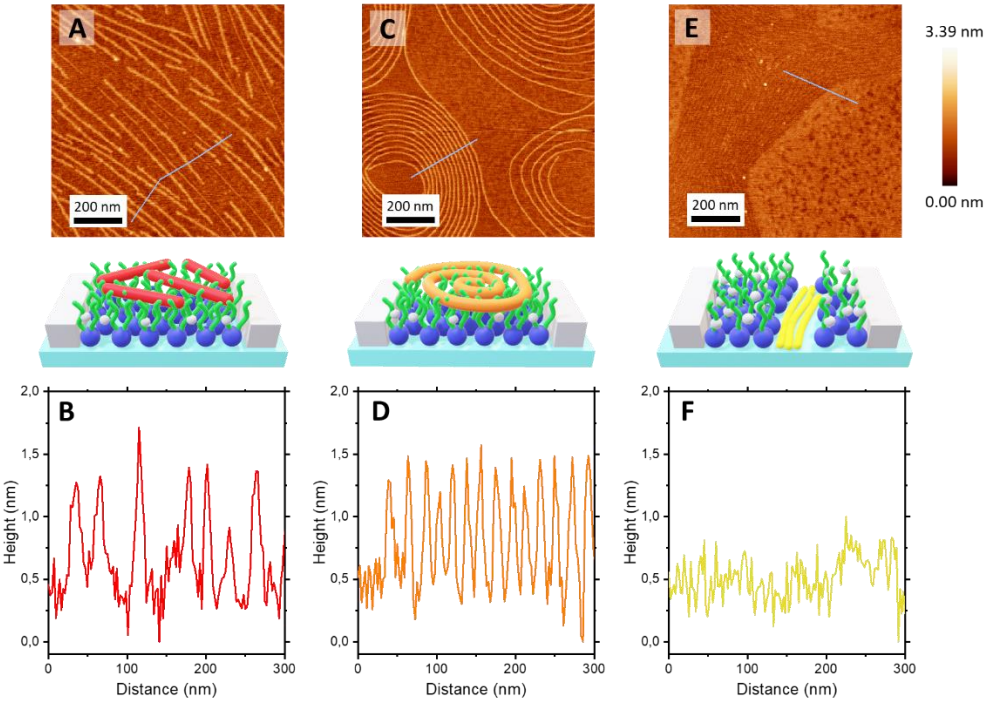

Figure 3. AFM topographical micrographs and corresponding topographical profiles of PM-FP1 (A, B), PM-FP2 (C, D), and PM-FP4 (E, F) at 20 mN/m surface pressure onto mica substrate. Schematic representations of the corresponding AFM images are also presented for clarity.

Due to FP1's high hydrophobicity,[11] the fibers mainly interact with the lipidic acyl chains of the PM. This is further supported by the topographical profiles in **Figure 3B**, which show that the FP1 fibers are partially located in the acyl chains region of the PM rather than integrated within the lipid headgroups region. These observations are consistent with FP1 preferentially interacts with the hydrophobic acyl chain region rather than with the polar headgroups.[11] In contrast to isolated FP1 spirals, the fibril height observed here in the presence of the PM monolayer (H = 1 ± 0.2 nm) is notably smaller than the height of 2.0 nm reported for a pure FP1 monolayer.[6] This discrepancy suggests that the FP1 fibers are partially integrated into the PM. This is likely driven by the interplay of steric and non-covalent interactions mediated by the peptide's amino acid sequence. Hydrophobic residues within FP1 preferentially interact

with the lipid acyl chains, while its more hydrophilic residues are likely to remain outside the PM. These findings indicate that at pressure characteristics of the LE phase, FP1 self-assembles into fibrillar structures on the PM interface. This behavior is governed by FP1´s secondary structure, assuming a β-strand configuration, as well as the lipid packing state.

In contrast, at Π = 35 mN/m where the PM adopts a condensed phase, the fibrillar structures observed at lower Π disappear, resulting in a more homogeneous topography (**Figures 4A** and **4B**). AFM topographical images reveal a minimal distribution of peptide fibers, compared to the noticeable fibrillar arrangement observed at Π = 20 mN/m. This transition suggests that the increased uniaxial compression forces at higher Π disrupt the peptides´ ability to maintain fibrillar self-assembly within the lipid acyl chains region, supports the hypothesis that increased surface compression induces a transition from fibrillar self-assembly to a state where the peptides either integrate into or embed within the lipid matrix. This integration may result from steric hindrance and tighter lipid packing in the C phase, which restrict the available space for peptide aggregation at the interface. Moreover, the loss of fibrillar structures may reflect a shift in the intricate balance of stabilizing interactions, such as van der Waals, and electrostatic interactions, which are predominant in the LE regime.

These results suggest that the lipid packing state not only influences FP1's structural organization but also modulates its functional role at the PM. By altering interaction dynamics with the lipid matrix, the PM's phase state may impact on the stability and assembly of FP1, potentially affecting its biological activity.

3.3.2.- Twisting into Spirals: FP2 forms into Flexible Nanofibers on PM Monolayers

AFM topographical micrograph of the PM in the presence of FP2 at a Π of 20 mN/m shows a network of elongated and flexible nanofibrils, arranged into distinctive spiral assemblies on the PM (**Figure 2C** and **S5B**). This suggests cooperative interactions between fibers during FP2 self-assembly, potentially driven by specific intermolecular forces and/or steric compatibility, as also observed with FP1.

The spiral fibril heights for FP2 (H = 1.2 ± 0.2 nm) indicate a fibrillar structure with backbones aligned parallel to the surface (**Figure 3D**), interacting partially with the lipid acyl chain region of the PM monolayer, which is similar to FP1. Molecular size calculations for FP2, assuming a β-strand structure, predict dimensions of approximately 8.1 nm in length and 1.5 nm in height, consistent with the observed fibril dimensions. Previous studies on FP2 demonstrated that β-sheet structures enhance the peptide's ability to generate fibres arranged in a spiral fashion at

fluid interfaces.[6] Like FP1, FP2 predominantly interacts with the hydrophobic tail regions of the lipids in the PM, driven by hydrophobic interactions. However, unlike FP1 —characterized by a higher content of hydrophobic residues such as Leu, Ile, and Val, resulting in the formation of straight fibrils with rigid morphologies— FP2 contains a mix of charged and polar residues, including Lys, Asp, and Gln. These residues can selectively disrupt the β-sheet structure due to electrostatic repulsion and solvation effects, leading to the formation of flexible fibrils that rearrange into spirals. Additionally, the presence of cysteine residues, capable of forming disulfide bonds, could facilitate the unique spiral assemblies observed at the PM interface.

Variations in the rigidity of FP1 and FP2 fibrils are evident in the AFM micrographs shown in **Figures 3A** and **3B**. FP1 fibrils are significantly longer and exhibit minimal curvature, whereas FP2 fibrils display a pronounced tendency to curve, folding into complex nanospiral structures. Quantitative analysis of fibril curvature, presented in **Figure S6**, reveals a curvature angle of 175 ± 6° for FP1 fibrils, indicative of their rigidity, compared to FP2 fibrils, which show a reduced curvature angle of 164 ± 7° at Π = 20m N/m. To further characterize these differences, FP1 and FP2 fibrils were modelled as worm-like chains, and their persistence lengths (Lp) were calculated based on the relationship between contour length and end-to-end distance (SI and **Figure S7**).[6] In the presence of the PM monolayer, FP1 fibrils displayed a Lp of 0.55 ± 0.02 μm, while FP2 fibrils exhibited a lower Lp of 0.15 ± 0.03 μm, indicating greater flexibility. Interestingly, these persistence length values are remarkably similar to those obtained for FP1 (3.2 ± 0.2 μm) and FP2 (0.12 ± 0.03 μm) in the absence of lipids.[6] The similarity between these values suggests that the intrinsic mechanical properties of FP1 and FP2 fibrils, such as stiffness and flexibility, are primarily dictated by their peptide structure and are only minimally influenced by the lipid environment at this surface pressure.

Similar to FP1, increasing the Π to 35 mN/m resulted in the partial disappearance of peptide fibrils from the PM surface (**Figure 4C** and **4D**). Instead, short fibres arranged in circular patterns remain on the PM, acting as remnants or "patch marks" of the previously observed spiral assemblies. The disassembly of the spirals is likely driven by steric constraints and the lateral compression of the surrounding lipids, which disrupt the structural integrity of the spirals and promote their reorganization. This is further supported by the reduction in the area per molecule occupied by FP2, as indicated by the Π - A isotherm (**Figure 1D**). Notably, in the absence of lipids, the spirals remained intact, suggesting that lipid interactions and the associated steric hindrance are key factors driving spiral disassembly under compression.[6]

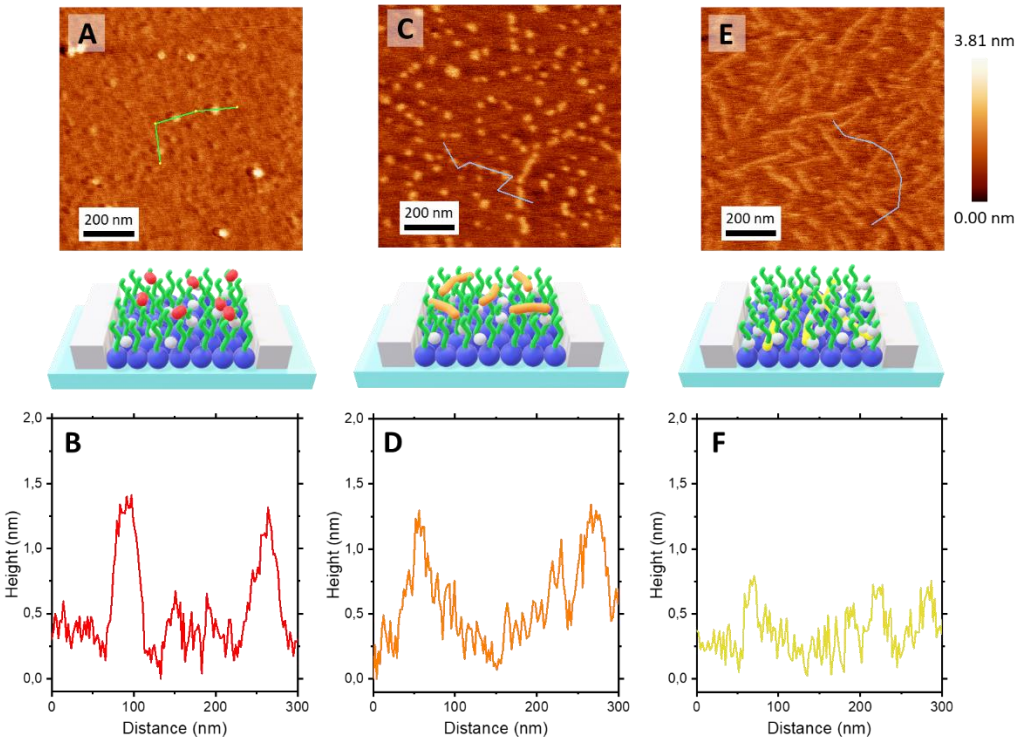

Figure 4. AFM topographical micrographs and corresponding topographical profiles of PM-FP1 (A, B), PM-FP2 (C, D), and PM-FP4 (E, F) at 35 mN/m surface pressure onto mica substrate. Schematic representations of the corresponding AFM images are also presented for clarity.

3.3.3- Electrostatic Stabilization and Structural Resilience of FP4 Fibrils on PM Monolayers

The strong affinity of FP4 for the PM is primarily driven by electrostatic interactions between the peptide's overall positive charge and the negatively charged polar heads of the PM phospholipids [11]. This affinity is further confirmed by the Π-A isotherms in **Figure 1D,** which show significant changes to the lipid monolayer upon the introduction of FP4.

The AFM micrographs in **Figure 3E** (and **Figure S5C**) show that FP4 induces phase separation in the PM, resulting in two different regions. One is enriched in peptide fibers that align in a parallel fashion, and the other consists of phospholipids and cholesterol, with both *Lo* and *Ld* domains also visible. The negligible difference in height between the lipidic domains and the FP fibers (**Figure 3F**) suggests a complete phase segregation regime, with the FP4 fibers localized between the lipid domains rather than integrated on them, distinguishing their behavior from that of FP1 and FP2.

The assembly of FP4 into short, linear fibrils can be attributed to its β-sheet secondary structure in the presence of membranes, as previously confirmed by circular dichroism experiments.[11]

The ordered organization of the fibrils at the lipid interface is responsible for the observed phase separation, as it locally disrupts the lipid packing and forms distinct peptide-rich domains. Additionally, the parallel alignment of FP4 fibrils on the membrane can be further by the glycine-rich regions in FP4, which promote increased backbone flexibility, allowing the peptide to adopt extended conformations and facilitating the formation of well-organized β-sheet structures. This flexibility is key to enabling the fibrils to pack tightly and align in parallel, promoting the formation of ordered superstructures. Aromatic residues in FP4 also play a significant role in stabilizing the parallel alignment of the fibrils. These residues can engage in π-π stacking interactions, providing additional stabilization and promoting the fibrils to align in parallel. In contrast, FP1 and FP2, which lack both the glycine-rich sequences and the same level of aromatic stacking potential, are less able to form such highly ordered parallel structures.

The persistence of FP4 fibers within the PM monolayer at Π = 35 mN/m contrasts with FP1 and FP2, where higher Π led to the disassembly of peptide structures from the membrane. AFM topographical images (**Figures 4E** and **4F**) reveal that FP4 fibrils remain integrated into the PM monolayer under these conditions, with uniaxial compression promoting the merging of previously segregated peptide-rich and lipid-rich domains.

3.3. *Study of the impact of FP on PM adhesive properties by AFM.*

To further validate previous observations, the adhesive forces of the PM and FP monolayers were investigated using AFM in QNM mode. Adhesive forces, which measure the attractive interactions between the AFM probe tip and the sample surface, provide additional details on the interaction dynamics at the molecular level.

Figure 5 presents the adhesive force mapping for the samples studied during this work at Π of 20 and 35 mN/m. At Π= 20 mN/m, adhesive forces of approximately 1.6 nN were observed for the pristine PM, and these values remained relatively constant upon the addition of the FPs. This consistency suggests that the FPs do not significantly alter the adhesive properties of the PM at these surface pressures, implying that the FPs are more likely segregated from the PM rather than integrated into it. For FP1 and FP2 (**Figures 5B** and **5C**, respectively), fibers are clearly visible in the adhesive force images, exhibiting minimal adhesive force values due to their completely hydrophobic nature. This observation supports the topography findings, confirming that FP fibers form at the tail part of the PM monolayer. In contrast, for FP4 (**Figure**

5D), large areas of FP domains were detected, corresponding to the extensive fiber regions observed in **Figure 3E**. This observation, combined with the negligible differences in topography, further confirms that FP4 and the lipid monolayer segregate into distinct domains.

When Π increased to 35 mN/m, the aggregation of the SM and cholesterol, suggested by the topography images, was confirmed in the adhesive force images for the pristine PM (**Figure 5E**). Areas of minimal adhesive forces were detected, corresponding to the cholesterol and SM hydrophobic domains. The increased surface pressure also impacts FP self-assembly, as previously noted. For FP1 (**Figure 5F**) and FP2 (**Figure 5G**) PMs, no fibers were detected, indicating that the peptides integrate into the membrane at higher surface pressures, leading to the disassembly of the previously observed fibers. Additionally, no cholesterol and SM aggregation were observed, which is consistent with GIXD data, further confirming that FPs inhibit the segregation of these components. In the case of FP4, the increased packing of the PM due to higher compressive forces facilitated the homogeneous integration of fibers into the membrane (**Figure 5H**).

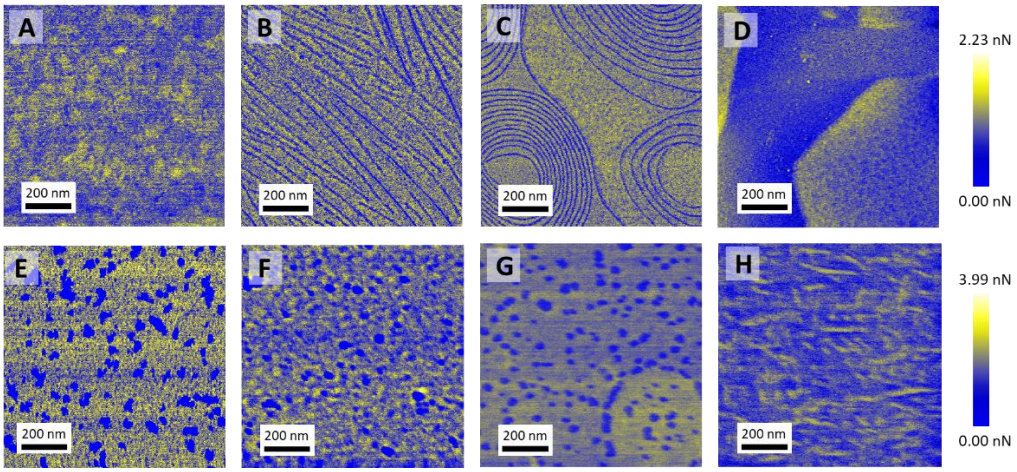

Figure 5. AFM adhesive force maps of the pristine PM monolayer (A, E), PM-FP1 (B, F), PM-FP2 (C, G), and PM-FP4 (D, H) at 20 mN/m (top) and 35 mN/m (bottom) surface pressure onto mica substrate.

4. Discussion and conclusions:

Understanding the fusion domain of the SARS-CoV-2 spike protein using *in vitro* model membranes is an important step in unraveling the molecular mechanisms of viral entry. Here, three distinct peptide sequences (FP1, FP2, and FP4) of the fusion domain were systematically investigated. Their interactions with lipid monolayers that mimic the outer leaflet of the eukaryotic plasma membrane, allowed us to evaluate how variations in sequence influence

membrane affinity, their structural organization within the monolayer, and their capacity to self-assemble into distinct architectures.

SARS-CoV-2 FPs have shown very different assembly behaviors in the presence of biomimetic PMs. Despite having similar numbers of amino acids and molecular weights (**Table S1**), their unique amino acid sequences predominantly dictate the formation of self-assembled structures on the PM. Differences in net charge and hydrophobicity further contributed to these assembly variations. Additionally, the secondary structure of the FPs plays a crucial role in guiding these self-assembled structures. Thus, the interaction of FPs with PM is evidenced by changes in area per molecule (**Figures 1D**) and varying topography and adhesive forces observed via AFM (**Figures 3, 4**, and **5**). During this interaction, the fusion peptides primarily associate with the lipids, excluding the cholesterol domains within the mixture (as confirmed by GIXD, **Figures 1G** and **1H**).

Previous studies have already demonstrated the preference of FP1 for the hydrophobic acyl region, as also observed in these experiments. FP1 contains a non-polar motif, Leu-Leu-Phe (LLF), which plays a critical role in membrane fusion.[40–42] The hydrophobic nature of LLF promotes FP1´s interactions with acyl chains of lipids in the PM.[43–45] Our results demonstrated that in monolayer models at the LE state (Π = 20mN/m), FP1 tends to form fibres in the hydrophobic acyl regions, which coexist with domains rich in lipids, ~~cholesterol, and FP1 monomers~~. A similar coexistence of peptide fibres and circular structures has been observed in DSPC bilayers.[46] The association of the secondary structure (β-sheet) results in the formation of long fibres (see **Figure 3A**). Increasing the Π to 35 mN/m enhances the hydrophobic interactions between FP1 and the lipids, enabling the peptide to penetrate deeper into the membrane (**Figure 4A**).

FP2 exhibits a remarkable response towards the biomimetic PM by forming spiral assemblies at the interface (**Figure 3C**), a distinctive behavior among the fusion peptides studied. The secondary structure of FP2 plays a key role in this self-assembly process, particularly through interactions with the hydrophobic acyl region of the lipids via key hydrophobic forces. Notably, the secondary structure of FP2 remains unchanged after interacting with the lipids, as molecular dynamic simulations have demonstrated its capability to wrap around negatively charged phospholipids without significant alteration.[36] Hence, the β-sheet structure present in FP2 is crucial for its self-assembly into fibres. The application of uniaxial compressive forces by LB further enhances packing density, thereby increasing excluded volume interactions among the

peptide and facilitating fibre elongation.[47,48] This phenomenon is also observed in other peptides like melittin or silk-derived peptides, which are known to form secondary structures, particularly β-sheets, at the air/water interface.[46,49]. With a further increase in surface pressure to 35 mN/m, the disassembly of the fibres occurs (**Figure 4C**), suggesting that the peptides integrate deeper into the PM or may even be excluded from it, as suggested by the merge of the Π-A isotherms (**Figure 1D**)

FP4 has demonstrated a larger binding affinity towards the PM,[11] primarily driven by electrostatic interactions with the polar headgroups of lipids and hydrophobic forces with the alkyl chains of the lipids. The balance between these interactions is critical for tuning its self-assembly on the monolayer. Additionally, the application of uniaxial pressure by LB techniques increases excluded volume interactions, further influencing peptide-peptide interactions. Thus, at a surface pressure of 20 mN/m, which mimics the LE of lipids, peptide interactions with the lipid heads dominate, leading to phase separation (**Figure 3E**). As the surface pressure increases to 35 mN/m and the available surface area decreases, FP4 peptide fibres integrate into the PM membrane (**Figure 4E**). This integration indicates a favorable interactionbetween FP4 and the PM lipids, as suggested by the Π-A isotherms (**Figure 1D**) and confirmed also by previous studies.[11]

In conclusion, a range of biophysical techniques was used to investigate the interaction of SARS-CoV-2 fusion peptides with model plasma membranes. The fusion peptides undergo conformational changes, forming stable, flexible fibers assembly at the membrane interface. These findings offer crucial insights into the membrane fusion process, a critical step in viral infection. Moreover, we demonstrated how increased lipid packing density influence peptide self-assembly on the membrane, shedding light on the underlying mechanism of viral fusion [Nathan: which one?]. This work provides also a foundation for developing advanced drug delivery systems and other biomedical applications by exploiting the dual role of peptide self-assembly, serving both as a structural platform and a modulator of lipid organization.

Acknowledgements

The authors thank the Institute Laue-Langevin (ILL) for allocation of neutron beam time on FIGARO (DOI: 10.5291/ILL-DATA.DIR-215) and the European Synchrotron Radiation Facility (ESRF) for provision of synchrotron radiation facilities in beamline ID10 under proposal number LS3159 (DOI:10.15151/ESRF-ES-883953841). We acknowledge O.

Konovalov for his valuable assistance during the GIXD experiments. A.M. and E.G. acknowledge the financial support from by MCIN/AEI/10.13039/501100011033 under grants PID2021-129054NA-I00 and PID2023-147156NB-I00, respectively. A.M. also acknowledges the financial support from the Department of Education of the Basque Government under grant PIBA_2023_1_0054 and from the IKUR Strategy under the collaboration agreement between Ikerbasque Foundation and Materials Physics Center. AAF is grateful for support from the Provincial Council of Gipuzkoa under the program Fellow Gipuzkoa. E.G. also acknowledges the financial support by UCM under grant PR12/24-31566 (Ayudas para la financiación de proyectos de investigación UCM 2023).

References:

(1) Chiliveri, S. C.; Louis, J. M.; Ghirlando, R.; Bax, A. Transient Lipid-Bound States of Spike Protein Heptad Repeats Provide Insights into SARS-CoV-2 Membrane Fusion. *Sci Adv* **2021**, *7* (41). https://doi.org/10.1126/sciadv.abk2226.

(2) Shi, W.; Cai, Y.; Zhu, H.; Peng, H.; Voyer, J.; Rits-Volloch, S.; Cao, H.; Mayer, M. L.; Song, K.; Xu, C.; Lu, J.; Zhang, J.; Chen, B. Cryo-EM Structure of SARS-CoV-2 Postfusion Spike in Membrane. *Nature 2023 619:7969* **2023**, *619* (7969), 403–409. https://doi.org/10.1038/s41586-023-06273-4.

(3) Li, Q.; Wu, J.; Nie, J.; Zhang, L.; Hao, H.; Liu, S.; Zhao, C.; Zhang, Q.; Liu, H.; Nie, L.; Qin, H.; Wang, M.; Lu, Q.; Li, X.; Sun, Q.; Liu, J.; Zhang, L.; Li, X.; Huang, W.; Wang, Y. The Impact of Mutations in SARS-CoV-2 Spike on Viral Infectivity and Antigenicity. *Cell* **2020**, *182* (5), 1284-1294.e9. https://doi.org/10.1016/J.CELL.2020.07.012.

(4) Daly, J. L.; Simonetti, B.; Klein, K.; Chen, K. E.; Williamson, M. K.; Antón-Plágaro, C.; Shoemark, D. K.; Simón-Gracia, L.; Bauer, M.; Hollandi, R.; Greber, U. F.; Horvath, P.; Sessions, R. B.; Helenius, A.; Hiscox, J. A.; Teesalu, T.; Matthews, D. A.; Davidson, A. D.; Collins, B. M.; Cullen, P. J.; Yamauchi, Y. Neuropilin-1 Is a Host Factor for SARS-CoV-2 Infection. *Science (1979)* **2020**, *370* (6518), 861–865. https://doi.org/10.1126/SCIENCE.ABD3072/SUPPL_FILE/ABD3072_REPRODUCIBILITYCHECKLIST.PDF.

(5) Gallagher, T. M.; Buchmeier, M. J. Coronavirus Spike Proteins in Viral Entry and Pathogenesis. *Virology* **2001**, *279* (2), 371–374. https://doi.org/10.1006/viro.2000.0757.

(6) Alvarez-Fernandez, A.; Pawar, N.; Sanchez-Puga, P.; Zaccai, Nathan. R.; Maestro, A. Peptide-Guided Self-Assembly: Fabrication of Tailored Spiral-Like Nanostructures for Precise Inorganic Templating. *Adv Funct Mater* **2024**. https://doi.org/10.1002/adfm.202411061.

(7) Li, W.; Moore, M. J.; Vasllieva, N.; Sui, J.; Wong, S. K.; Berne, M. A.; Somasundaran, M.; Sullivan, J. L.; Luzuriaga, K.; Greeneugh, T. C.; Choe, H.; Farzan, M. Angiotensin-Converting

Enzyme 2 Is a Functional Receptor for the SARS Coronavirus. *Nature 2003 426:6965* **2003**, *426* (6965), 450–454. https://doi.org/10.1038/nature02145.

(8) Shang, J.; Wan, Y.; Luo, C.; Ye, G.; Geng, Q.; Auerbach, A.; Li, F. Cell Entry Mechanisms of SARS-CoV-2. *Proc Natl Acad Sci U S A* **2020**, *117* (21). https://doi.org/10.1073/PNAS.2003138117.

(9) Yu, J.; Zhang, Z. W.; Yang, H. Y.; Liu, C. J.; Lu, W. C. Study of Fusion Peptide Release for the Spike Protein of SARS-CoV-2. *RSC Adv* **2023**, *13* (25), 16970–16983. https://doi.org/10.1039/D3RA01764H.

(10) Kielian, M.; Rey, F. A. Virus Membrane-Fusion Proteins: More than One Way to Make a Hairpin. *Nature Reviews Microbiology 2006 4:1* **2006**, *4* (1), 67–76. https://doi.org/10.1038/nrmicro1326.

(11) Santamaria, A.; Batchu, K. C.; Matsarskaia, O.; Prévost, S. F.; Russo, D.; Natali, F.; Seydel, T.; Hoffmann, I.; Laux, V.; Haertlein, M.; Darwish, T. A.; Russell, R. A.; Corucci, G.; Fragneto, G.; Maestro, A.; Zaccai, N. R. Strikingly Different Roles of SARS-CoV-2 Fusion Peptides Uncovered by Neutron Scattering. *J Am Chem Soc* **2022**, *144* (7), 2968–2979. https://doi.org/10.1021/JACS.1C09856/ASSET/IMAGES/LARGE/JA1C09856_0005.JPEG.

(12) Low, J. S.; Jerak, J.; Tortorici, M. A.; McCallum, M.; Pinto, D.; Cassotta, A.; Foglierini, M.; Mele, F.; Abdelnabi, R.; Weynand, B.; Noack, J.; Montiel-Ruiz, M.; Bianchi, S.; Benigni, F.; Sprugasci, N.; Joshi, A.; Bowen, J. E.; Stewart, C.; Rexhepaj, M.; Walls, A. C.; Jarrossay, D.; Morone, D.; Paparoditis, P.; Garzoni, C.; Ferrari, P.; Ceschi, A.; Neyts, J.; Purcell, L. A.; Snell, G.; Corti, D.; Lanzavecchia, A.; Veesler, D.; Sallusto, F. ACE2-Binding Exposes the SARS-CoV-2 Fusion Peptide to Broadly Neutralizing Coronavirus Antibodies. *Science (1979)* **2022**, *377* (6607), 735–742. https://doi.org/10.1126/science.abq2679.

(13) Dacon, C.; Tucker, C.; Peng, L.; Lee, C.-C. D.; Lin, T.-H.; Yuan, M.; Cong, Y.; Wang, L.; Purser, L.; Williams, J. K.; Pyo, C.-W.; Kosik, I.; Hu, Z.; Zhao, M.; Mohan, D.; Cooper, A. J. R.; Peterson, M.; Skinner, J.; Dixit, S.; Kollins, E.; Huzella, L.; Perry, D.; Byrum, R.; Lembirik, S.; Drawbaugh, D.; Eaton, B.; Zhang, Y.; Yang, E. S.; Chen, M.; Leung, K.; Weinberg, R. S.; Pegu, A.; Geraghty, D. E.; Davidson, E.; Douagi, I.; Moir, S.; Yewdell, J. W.; Schmaljohn, C.; Crompton, P. D.; Holbrook, M. R.; Nemazee, D.; Mascola, J. R.; Wilson, I. A.; Tan, J. Broadly Neutralizing Antibodies Target the Coronavirus Fusion Peptide. *Science (1979)* **2022**, *377* (6607), 728–735. https://doi.org/10.1126/science.abq3773.

(14) Brockman, H. Lipid Monolayers: Why Use Half a Membrane to Characterize Protein-Membrane Interactions? *Curr Opin Struct Biol* **1999**, *9* (4), 438–443. https://doi.org/10.1016/S0959-440X(99)80061-X.

(15) Krajewska, M.; Dopierała, K.; Prochaska, K. Lipid-Protein Interactions in Langmuir Monolayers under Dynamically Varied Conditions. *Journal of Physical Chemistry B* **2020**, *124* (1), 302–311. https://doi.org/10.1021/ACS.JPCB.9B10351/ASSET/IMAGES/LARGE/JP9B10351_0004.JPEG.

(16) Ingólfsson, H. I.; Melo, M. N.; van Eerden, F. J.; Arnarez, C.; Lopez, C. A.; Wassenaar, T. A.; Periole, X.; de Vries, A. H.; Tieleman, D. P.; Marrink, S. J. Lipid Organization of the Plasma Membrane. *J Am Chem Soc* **2014**, *136* (41), 14554–14559. https://doi.org/10.1021/ja507832e.

(17) Corucci, G.; Batchu, K. C.; Luchini, A.; Santamaria, A.; Frewein, M. P. K.; Laux, V.; Haertlein, M.; Yamaryo-Botté, Y.; Botté, C. Y.; Sheridan, T.; Tully, M.; Maestro, A.; Martel, A.; Porcar, L.;

Fragneto, G. Developing Advanced Models of Biological Membranes with Hydrogenous and Deuterated Natural Glycerophospholipid Mixtures. *J Colloid Interface Sci* **2023**, *645*, 870–881. https://doi.org/10.1016/j.jcis.2023.04.135.

(18) Santamaria, A.; Batchu, K. C.; Fragneto, G.; Laux, V.; Haertlein, M.; Darwish, T. A.; Russell, R. A.; Zaccai, N. R.; Guzmán, E.; Maestro, A. Investigation on the Relationship between Lipid Composition and Structure in Model Membranes Composed of Extracted Natural Phospholipids. *J Colloid Interface Sci* **2023**, *637*, 55–66. https://doi.org/10.1016/j.jcis.2023.01.043.

(19) Campbell, R. A.; Wacklin, H. P.; Sutton, I.; Cubitt, R.; Fragneto, G. FIGARO: The New Horizontal Neutron Reflectometer at the ILL. *The European Physical Journal Plus* **2011**, *126* (11), 107. https://doi.org/10.1140/epjp/i2011-11107-8.

(20) Gutfreund, P.; Saerbeck, T.; Gonzalez, M. A.; Pellegrini, E.; Laver, M.; Dewhurst, C.; Cubitt, R. Towards Generalized Data Reduction on a Chopper-Based Time-of-Flight Neutron Reflectometer. *J Appl Crystallogr* **2018**, *51* (3), 606–615. https://doi.org/10.1107/S160057671800448X.

(21) Campbell, R. A.; Tummino, A.; Noskov, B. A.; Varga, I. Polyelectrolyte/Surfactant Films Spread from Neutral Aggregates. *Soft Matter* **2016**, *12* (24), 5304–5312. https://doi.org/10.1039/C6SM00637J.

(22) Nelson, A. R. J.; Prescott, S. W. Refnx: Neutron and X-Ray Reflectometry Analysis in Python. *J Appl Crystallogr* **2019**, *52* (1), 193–200. https://doi.org/10.1107/S1600576718017296/RG5158SUP3.PDF.

(23) Braslau, A.; Deutsch, M.; Pershan, P. S.; Weiss, A. H.; Als-Nielsen, J.; Bohr, J. Surface Roughness of Water Measured by X-Ray Reflectivity. *Phys Rev Lett* **1985**, *54* (2), 114–117. https://doi.org/10.1103/PhysRevLett.54.114.

(24) Maestro, A.; Gutfreund, P. In Situ Determination of the Structure and Composition of Langmuir Monolayers at the Air/Water Interface by Neutron and X-Ray Reflectivity and Ellipsometry. *Adv Colloid Interface Sci* **2021**, *293*, 102434. https://doi.org/10.1016/J.CIS.2021.102434.

(25) Pittenger, B.; Slade, A. Performing Quantitative Nanomechanical AFM Measurements on Live Cells. *Micros Today* **2013**, *21* (6), 12–17. https://doi.org/10.1017/S1551929513001077.

(26) Gómez-Rodríguez, J. M.; Horcas, I.; Gómez-Herrero, J.; Baro, A. M.; Colchero, J.; Fernández, R. WSXM : A Software for Scanning Probe Microscopy and a Tool for Nanotechnology. *Review of Scientific Instruments* **2007**, *78* (1), 013705. https://doi.org/10.1063/1.2432410.

(27) Kjaer, K.; Als-Nielsen, J.; Helm, C. A.; Laxhuber, L. A.; Möhwald, H. Ordering in Lipid Monolayers Studied by Synchrotron X-Ray Diffraction and Fluorescence Microscopy. *Phys Rev Lett* **1987**, *58* (21), 2224. https://doi.org/10.1103/PhysRevLett.58.2224.

(28) Brezesinski, G.; Möhwald, H. Langmuir Monolayers to Study Interactions at Model Membrane Surfaces. *Adv Colloid Interface Sci* **2003**, *100–102* (SUPPL.), 563–584. https://doi.org/10.1016/S0001-8686(02)00071-4.

(29) Guo, X.; Briscoe, W. H. Molecular Interactions, Elastic Properties, and Nanostructure of Langmuir Bacterial-Lipid Monolayers: Towards Solving the Mystery in Bacterial Membrane

Asymmetry. *Curr Opin Colloid Interface Sci* **2023**, *67*, 101731. https://doi.org/10.1016/J.COCIS.2023.101731.

(30) Iimura, K.; Miguchi, M.; Ooshida, S.; Aizawa, Y.; Kato, T.; Brezesinski, G. Structures of Pure and Mixed Monolayers of Cholesterol and GM1 Studied by Grazing Incidence X -Ray Diffraction. *Transactions of the Materials Research Society of Japan* **2007**, *32* (1), 247–250. https://doi.org/10.14723/tmrsj.32.247.

(31) Flasiński, M.; Broniatowski, M.; Majewski, J.; Dynarowicz-Łątka, P. X-Ray Grazing Incidence Diffraction and Langmuir Monolayer Studies of the Interaction of β-Cyclodextrin with Model Lipid Membranes. *J Colloid Interface Sci* **2010**, *348* (2), 511–521. https://doi.org/10.1016/j.jcis.2010.04.086.

(32) Zaborowska, M.; Broniatowski, M.; Fontaine, P.; Bilewicz, R.; Matyszewska, D. Statin Action Targets Lipid Rafts of Cell Membranes: GIXD/PM-IRRAS Investigation of Langmuir Monolayers. *J Phys Chem B* **2023**, *127* (32), 7135–7147. https://doi.org/10.1021/acs.jpcb.3c02574.

(33) Pawlowska, D.; Janich, C.; Langner, A.; Dobner, B.; Wölk, C.; Brezesinski, G. The Impact of Alkyl-Chain Purity on Lipid-Based Nucleic Acid Delivery Systems – Is the Utilization of Lipid Components with Technical Grade Justified? *ChemPhysChem* **2019**, *20* (16), 2110–2121. https://doi.org/10.1002/CPHC.201900480.

(34) Guo, X. Y.; Yi, L.; Yang, J.; An, H. W.; Yang, Z. X.; Wang, H. Self-Assembly of Peptide Nanomaterials at Biointerfaces: Molecular Design and Biomedical Applications. *Chemical Communications* **2024**, *60* (15), 2009–2021. https://doi.org/10.1039/D3CC05811E.

(35) Wydro, P.; Flasiński, M.; Broniatowski, M. Grazing Incidence X-Ray Diffraction and Brewster Angle Microscopy Studies on Domain Formation in Phosphatidylethanolamine/Cholesterol Monolayers Imitating the Inner Layer of Human Erythrocyte Membrane. *Biochimica et Biophysica Acta (BBA) - Biomembranes* **2013**, *1828* (6), 1415–1423. https://doi.org/10.1016/J.BBAMEM.2013.01.023.

(36) Villalaín, J. SARS-CoV-2 Protein S Fusion Peptide Is Capable of Wrapping Negatively-Charged Phospholipids. *Membranes (Basel)* **2023**, *13* (3), 344. https://doi.org/10.3390/MEMBRANES13030344/S1.

(37) Veatch, S. L.; Keller, S. L. Organization in Lipid Membranes Containing Cholesterol. *Phys Rev Lett* **2002**, *89* (26), 268101. https://doi.org/10.1103/PhysRevLett.89.268101.

(38) Pandit, S. A.; Vasudevan, S.; Chiu, S. W.; Mashl, R. J.; Jakobsson, E.; Scott, H. L. Sphingomyelin-Cholesterol Domains in Phospholipid Membranes: Atomistic Simulation. *Biophys J* **2004**, *87* (2), 1092–1100. https://doi.org/10.1529/BIOPHYSJ.104.041939.

(39) Taylor, S. E.; Desbat, B.; Blaudez, D.; Jacobi, S.; Chi, L. F.; Fuchs, H.; Schwarz, G. Structure of a Fusion Peptide Analogue at the Air–Water Interface, Determined from Surface Activity, Infrared Spectroscopy and Scanning Force Microscopy. *Biophys Chem* **2000**, *87* (1), 63–72. https://doi.org/10.1016/S0301-4622(00)00182-4.

(40) Lai, A. L.; Millet, J. K.; Daniel, S.; Freed, J. H.; Whittaker, G. R. The SARS-CoV Fusion Peptide Forms an Extended Bipartite Fusion Platform That Perturbs Membrane Order in a Calcium-Dependent Manner. *J Mol Biol* **2017**, *429* (24), 3875–3892. https://doi.org/10.1016/J.JMB.2017.10.017.

(41) Millet, J. K.; Whittaker, G. R. Physiological and Molecular Triggers for SARS-CoV Membrane Fusion and Entry into Host Cells. *Virology* **2018**, *517*, 3–8. https://doi.org/10.1016/J.VIROL.2017.12.015.

(42) Khelashvili, G.; Plante, A.; Doktorova, M.; Weinstein, H. Ca2+-Dependent Mechanism of Membrane Insertion and Destabilization by the SARS-CoV-2 Fusion Peptide. *Biophys J* **2021**, *120* (6), 1105–1119. https://doi.org/10.1016/J.BPJ.2021.02.023.

(43) Zhang, J.; Cai, Y.; Xiao, T.; Lu, J.; Peng, H.; Sterling, S. M.; Walsh, R. M.; Rits-Volloch, S.; Zhu, H.; Woosley, A. N.; Yang, W.; Sliz, P.; Chen, B. Structural Impact on SARS-CoV-2 Spike Protein by D614G Substitution. *Science (1979)* **2021**, *372* (6541), 525–530. https://doi.org/10.1126/SCIENCE.ABF2303/SUPPL_FILE/ABF2303_ZHANG_SM.PDF.

(44) Fu, Q.; Chou, J. J. A Trimeric Hydrophobic Zipper Mediates the Intramembrane Assembly of SARS-CoV-2 Spike. *J Am Chem Soc* **2021**, *143* (23), 8543–8546. https://doi.org/10.1021/JACS.1C02394/ASSET/IMAGES/LARGE/JA1C02394_0003.JPEG.

(45) Aydin, H.; Al-Khooly, D.; Lee, J. E. Influence of Hydrophobic and Electrostatic Residues on SARS-Coronavirus S2 Protein Stability: Insights into Mechanisms of General Viral Fusion and Inhibitor Design. *Protein Science* **2014**, *23* (5), 603–617. https://doi.org/10.1002/PRO.2442.

(46) Alvarez, A. B.; Caruso, B.; Petersen, S. B.; Rodríguez, P. E. A.; Fidelio, G. D. Melittin-Solid Phospholipid Mixed Films Trigger Amyloid-like Nano-Fibril Arrangements at Air-Water Interface. *Biochimica et Biophysica Acta (BBA) - Biomembranes* **2022**, *1864* (12), 184048. https://doi.org/10.1016/j.bbamem.2022.184048.

(47) Cicuta, P.; Terentjev, E. M. Viscoelasticity of a Protein Monolayer from Anisotropic Surface Pressure Measurements. *The European Physical Journal E 2005 16:2* **2005**, *16* (2), 147–158. https://doi.org/10.1140/EPJE/E2005-00016-Y.

(48) Ahmadi, S.; Kerman, K.; Uppal, M.; Mezzenga, R.; Fischer, P. The Self-Assembly, Aggregation and Phase Transitions of Food Protein Systems in One, Two and Three Dimensions. *Reports on Progress in Physics* **2013**, *76* (4), 046601. https://doi.org/10.1088/0034-4885/76/4/046601.

(49) Wen, H.; Yao, J.; Chen, X.; Ling, S.; Shao, Z. Silk-Derived Peptide Nanospirals Assembled by Self-Propelled Worm-like Filaments. *Nano Res* **2023**, *16* (1), 1414–1420. https://doi.org/10.1007/S12274-022-4671-1/METRICS.